An IMPROVED IMAGE REGISTRATION ALGORITHM FOR THERMAL INFRARED AND PANCHROMATIC IMAGE BASED ON GEOMETRIC STRUCTURAL PROPERTIES

Junfeng Xie [1], Xing Lv [1,2,*], Cun Chu [3], Ren Liu [1], Fan Mo [1],Binbo Li [1,4,5], Chenglong Wang [6]

[1] Land Satellite Remote Sensing Application Center, Beijing 100048, China
[2] . College of Geoscience and Surveying Engineering, China University of Mining and Technology − Beijing, Beijing 100083, China
[3] School of Geomatics Liaoning Technical University, Fuxin 123000, China
[4] College of Resource Environment and Tourism, Capital Normal University, Beijing 100048, China
[5] State Key Laboratory Incubation Base of Urban Environmental Processes and Digital Simulation, Capital Normal University, Beijing 100048, China
[6] School of Resource and Environmental Sciences, Wuhan University, Wuhan 430079, China
E-mail: junfeng_xie@163.com (J. Xie), sqt2200205115@student.cumtb.edu.cn (X.Lv), 2218255068@qq.com（C. Chu）1140003596@qq.com (R. Liu), mof@lasac.cn (F. Mo), 2200902167@cnu.edu.cn (B. Li), chenglongw@whu.edu.cn (C. Wang).

KEY WORDS: Heterogeneous image registration; phase consistency; geometric structural properties; CSS corner detection.

ABSTRACT:

In order to improve the image registration accuracy of heterogeneous remote sensing images with large radiation differences, an improved image registration algorithm for thermal infrared and panchromatic images is proposed. This method uses the phase consistency of intensity and direction to construct a geometric structure feature descriptor called the Histogram of Oriented Phase Congruency (HOPC) for image registration. It employs the Curvature Scale Space (CSS) corner detection to concentrate and extract feature points in contour areas, and defines a similarity metric (called HOPCn) based on the Euclidean distance between the descriptors for high-precision heterogeneous images registration. Five sets of panchromatic and thermal infrared images were selected for verification. The results show that the improved algorithm can match the homonymy points around the image contour, and the Correct Matching Rate (CMR) is improved by 2.7% and the Root Mean Square Error (RMSE) is improved by 3.7% compared to the original algorithm. This proves that the proposed method has good robustness under conditions of large radiation differences.

1. INTRODUCTION

With the rapid development of sensor technology, remote sensing imagery has become an important way to observe the Earth's surface (Foody et al., 2002). Remote sensing imagery can be classified into satellite imagery (Hu et al., 2021), aerial imagery (Rahaghi et al., 2019), and so on, which depends on the different platform carrying the sensor. According to the classification of sensors, remote sensing imagery can be classified into Multi-spectral remote sensing (Bai et al., 2023), Thermal remote sensing (Masouleh et al., 2019), LiDAR (Light Detection and Ranging) (Dematteis et al., 2018), and so on. Different types of remote sensing imagery are widely applied in various fields such as environment monitoring(Zhang et al., 2023, Zhang et al., 2023), resource exploration (Wang et al., 2020, Joshi et al., 2016) and urban planning(Li et al., 2013, Gong et al., 2020), agriculture application(Valero et al., 2013, Deng et al., 2018), etc. For example, Landsat data, an multispectral remote sensing image, can be used to draw forest cover change maps (Song et al., 2015); optical and synthetic aperture radar (SAR) data can be used to monitor vegetation and soil moisture conditions(Ramat et al., 2023); ICESat-2's single photon laser altimetry data, combined with Google satellite imagery data, can obtain building heights(Zhao et al., 2023); and thermal infrared remote sensing imagery data can be used to evaluate urban heat islands(Weng et al., 2009).

Different types of remote sensing imagery provide different information. Different dimensions information of target can be obtained from thermal infrared and visible spectral remote sensing due to their different imaging principles. Thermal remote sensing provides surface temperature information (Sobrino et al., 2004), while visible spectral remote sensing has higher resolution and can get object location and shape information (Blaschke et al., 2010). Stereo imaging can significantly improve the positioning accuracy of object (Gao et al., 2023). The fusion of optical and thermal infrared images can more effectively observe the earth's surface, further expanding the scope of remote sensing applications (Han et al., 2014). However, Prior to image fusion, it is necessary to perform image registration.

Image registration refers to aligning images of the same scene that are captured at different times, viewpoints, or by different sensors. (Zitova et al., 2003). It is a crucial step in remote sensing image processing and plays a vital role to improve the quality and reliability of remote sensing data (Ye et al., 2017). Scale invariant feature transform (SIFT) is a classic registration algorithm that was firstly proposed in the 1990s (Lowe D G., 2004) and has been widely used for registration of various images (Fischler et al., 1981). The algorithm can get good matching results for cross modality remote sensing images with consistent geographical locations and strong similarity in grayscale and structure (Yu et al., 2021). However, due to the different imaging methods and spectral characteristics of thermal remote sensing images and visible spectral remote sensing images, there is a large radiometric difference between thermal remote sensing images and visible spectral remote sensing images, and the registration effect of SIFT on cross modality remote sensing images is not satisfactory (Wang et al., 2022). Xi Shaoli et al. combined the SIFT operator with the Oriented Fast and Rotated Brief (ORB) operator, and by extracting a large number of feature points, they greatly improved the number and accuracy of matching points

* Corresponding author

(Xi et al., 2020). Duan Linfeng proposed an image registration method based on Nonsubsampled contourlet transform （NSCT）contour extraction and consistency matching of the main direction, which combined the 128-dimensional SIFT descriptor with the CSS algorithm to improve the accuracy of image registration. Yu Zhi et al. invented an image registration method based on feature contour quadrilaterals, and the experime.ntal results showed that this method can achieve more accurate contour positioning and efficient registration (Yu et al., 2021). Li Hongwei found contour feature points in the image based on the CSS algorithm, assigned a feature vector to each feature point for bilateral matching, and finally fused multiple feature information in the image (Li et al., 2022). Jiang Qian et al. improved the CSS algorithm to detect the edge of the image, then extracted the descriptor on the main direction of the feature point, performed image registration based on line consistency, and obtained the affine transformation relationship between the registered points to achieve image fusion. This method can achieve significant accuracy improvement compared with other registration algorithms (Jiang et al., 2020). Ye Yuanxin proposed an automatic registration algorithm based on geometric structure similarity, which can achieve high registration accuracy based on the structure of the image and can effectively solve the difficult registration problem of multimodal remote sensing images.

Due to the differences in sensors type, viewing angles, exposure times, and orbit heights between different satellites, such as visible spectral remote sensing satellites and thermal infrared remote sensing satellites, thermal infrared remote sensing and visible spectral remote sensing images captured in the same area often exhibit significant differences in radiation. Therefore, compared to image registration within the same satellite, thermal infrared remote sensing and visible spectral remote sensing images. matching from different satellites is more difficult, and traditional algorithms cannot achieve good matching results under these circumstances. To address these issues, this paper proposes a matching algorithm (Histogram of Orientated Phase Congreucy, HOPCSS) that combines the CSS detection operator with geometric structural feature descriptors. The algorithm first constructs the HOPC feature vectors of two images using phase congruency intensity and direction information, then extracts main image feature points using the CSS operator. After that, an affine transformation model is used to determine a search space of a certain size in the auxiliary image. The algorithm utilizes HOPCSS as a similarity metric for matching corresponding image points between the two images and finally employs the Random Sample Consensus (RANSAC) algorithm to eliminate mis-matching points, achieving the registration of thermal infrared remote sensing and visible spectral remote sensing images.

2. METHODOLOGY

2.1 Improved Infrared and visual Image Registration with HOPCSS

The HOPCSS algorithm process is briefly introduced by an explanation of the geometric structure descriptors, CSS corners, Harris (Harris Corner Detector) corners, and similarity metric .

The principle and process of the HOPCSS algorithm is shown in the figure 1. Firstly, geometric descriptors are constructed for the primary and secondary images. Then, the CSS feature points are extracted from the primary image, and the corresponding image point are detected using HOPCn. After that, an affine transformation model is used for registration, and the registration points with large errors are removed.

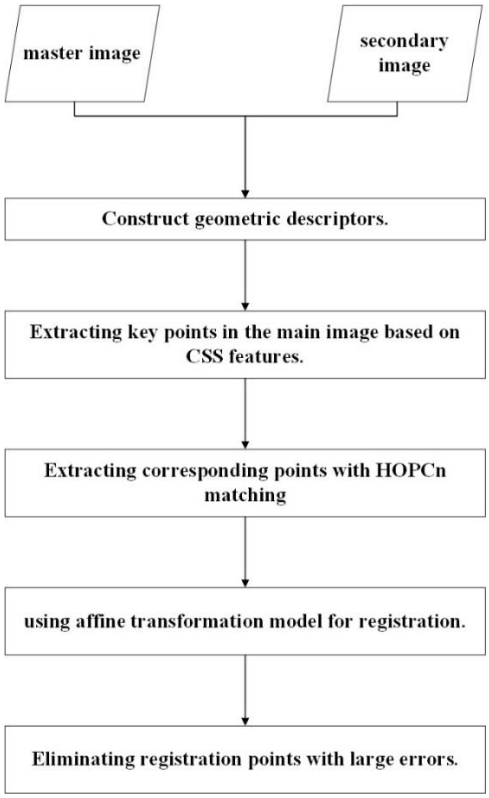

Figure 1. Registration Process of HOPCSS Algorithm

2.2 Construction of Geometric Descriptors

Firstly, HOPC descriptors are constructed by using phase congruency intensity and orientation information, and HOPCn is used to establish a similarity metric for image registration.

A. Strength of Phase Congruency.
The strength of phase congruency of the image is calculated using the Log Gabor wavelet with multiple orientations and scales (Kovesi ., 1999), and its mathematical expression is as follows:

$$PC(x,y)=\frac{\sum_{n}\sum_{o}W(x,y)\lfloor A_{no}(x,y)\Delta\Phi_{no}(x,y)-T\rfloor}{\sum_{n}\sum_{o}A_{no}(x,y)+\varepsilon} \quad (1)$$

Where $PC(x,y)$ represents the strength of phase congruency value of the pixel in the image, ε is a nonzero constant, $\lfloor\ \rfloor$ remains unchanged when $\lfloor\ \rfloor$ >0 and is 0 when $\lfloor\ \rfloor$ <0. T is the noise threshold, $A_{no}(x,y)$ is the amplitude of the pixel (x,y) on the log Gabor filter scale n and orientation o, which is multiplied by $\Delta\phi_{no}(x,y)$:

$$\begin{aligned}A_{no}(x,y)\Delta\Phi_{no}(x,y) &= (e_{no}(x,y)\overline{\phi_e}(x,y)+\\ o_{no}(x,y)\overline{\phi_o}(x,y))&-\left|e_{no}(x,y)\overline{\phi_o}(x,y)-o_{no}(x,y)\overline{\phi_e}(x,y)\right|\end{aligned} \quad (2)$$

Where

$$\overline{\phi_e}(x,y)=\sum_{n}\sum_{o}e_{no}(x,y)/E(x,y)$$

$$\overline{\phi_o}(x,y)=\sum_{n}\sum_{o}o_{no}(x,y)/E(x,y)$$

and $E(x,y)$ is a local energy function defined as follows:

$$\sqrt{(\sum_{n}\sum_{o} e_{no}(x,y))^2 + (\sum_{n}\sum_{o} o_{no}(x,y))^2} \quad (3)$$

In the equation, $e_{no}(x,y)$ and $o_{no}(x,y)$ are the even-symmetric and odd-symmetric filter signal response values of $Log\ Gabor$, respectively.

B. Orientation of Phase Congruency.

The Log Gabor filters can only obtain the strength of phase congruency values of the image, and geometric structure descriptors cannot be constructed solely based on phase congruency intensity values. It is also necessary to provide the orientation of phase congruency .

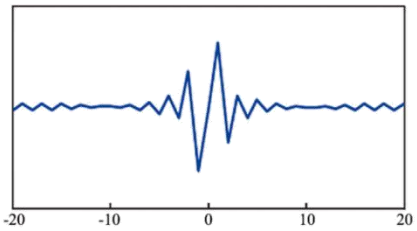

Figure 2. Log Gabor odd-symmetric filters.

The orientation of phase congruency represents the direction of the most drastic change in image features (similar to the gradient direction). It can be calculated using the odd-symmetric filter $o_{no}(x,y)$ of the Log Gabor wavelet. As shown in Figure 2.6, the odd-symmetric filter of the Log Gabor wavelet is similar to a derivative checking template, and its convolution result can represent the energy change of the image in a certain direction. When calculating phase congruency, multiple directions of Log Gabor odd-symmetric filters are used. Therefore, by projecting the odd-symmetric filter results onto the horizontal direction (X-axis) and vertical direction (Y-axis), the energy in the horizontal and vertical directions can be obtained respectively. Then, by calculating the value of inverse tangent function, the phase congruency feature direction Φ can be obtained, and the calculation formula is as follows:

$$\begin{aligned} a &= \sum_{\theta}(o_{no}(\theta)\cos(\theta)) \\ b &= \sum_{\theta}(o_{no}(\theta)\sin(\theta)) \\ \Phi &= \arctan(b,a) \end{aligned} \quad (4)$$

In the formula, $o_{no}(\theta)$ represents the response value of the odd-symmetric filter in direction θ.

C. Constructing geometric structure descriptors.

The specific process of constructing HOPC is shown in Figure 3, which mainly includes the following steps:

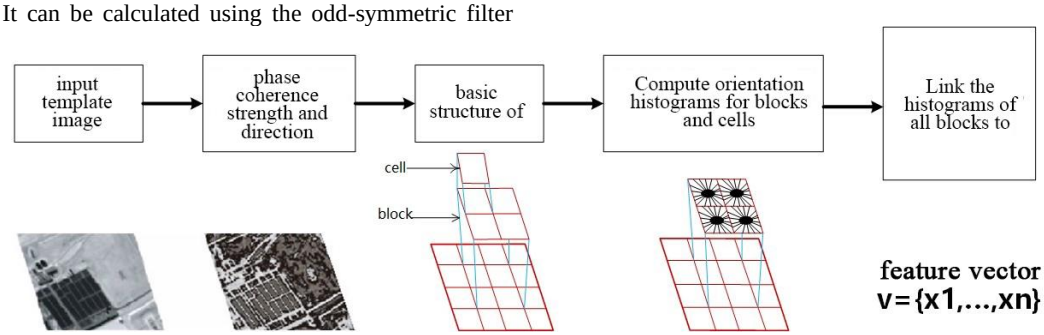

Figure 3. HOPC construction process

D. similarity metric

Considering the significant difference in brightness between the thermal infrared remote sensing and visible spectral remote sensing images , while their geometric structure features are relatively similar, the Euclidean distance between the HOPC descriptors is used as the similarity metric (HOPCn) for corresponding image point matching. The expression is as follows:

$$HOPC_n = \sqrt{\sum_{k=1}^{n}(V_A(k) - V_B(k))^2} \quad (5)$$

In the equation, V_A and V_B represent the HOPC descriptors of the template windows A and B, respectively.

2.3 Improvements in Corner Detection

Due to the fact that the matching algorithm based on geometric structural similarity proposed by Yuanxin Ye (HOPC algorithm) uses the Harris corner detection operator , which has good repeatability under rotation and various lighting conditions and is commonly used for stereo matching and image database retrieval, but is susceptible to noise and loss of localization accuracy, and is also sensitive to scale changes(Harris et al., 1988). However, the Harris algorithm tends to detect unnecessary feature point in blank areas of the image due to uniform sampling of the image. To address these shortcomings of the Harris algorithm, this paper adopts a new CSS corner detection algorithm, which includes the following main steps:

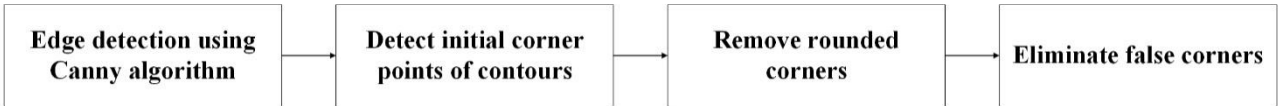

Figure 4. CSS corner detection process diagram.

A. Canny edge detection for edge extraction.

The Canny algorithm is an excellent image edge detection algorithm (Canny., 1986), but there is a problem of missing pixels in the process of edge extraction, which leads to the discontinuity of contours and T-shaped corner breaks. To solve this problem, it is necessary to process adjacent contours after edge extraction. If one end of an edge contour is close to another contour, they should be connected. If a contour is very close to

the middle part of an edge, the endpoint of the contour is regarded as a T-shaped corner. The following figure shows the process:

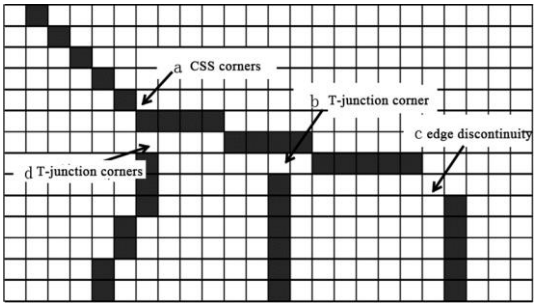

Figure 5. Schematic diagram of initial corner detection using CSS

After the above steps are completed, traverse all contours and detect the corners where the absolute value of curvature has a local maximum. These corners are regarded as the initial candidate corners. The contour curve is denoted as A, and its parameter form is given as:

$$\Gamma(t) = (x(t), y(t)) \tag{6}$$

For the curvature at point A on the edge, it can be obtained using the following equation:

$$k(t) = \frac{\dot{x}(t)\ddot{y}(t) - \dot{y}(t)\ddot{x}(t)}{\left(\dot{x}(t)^2 + \dot{y}(t)^2\right)^{3/2}} \tag{7}$$

B. Removing Rounded Corners

The initial list of candidate corners is $A^j = \{P_1^j, P_2^j, ..., P_N^j\}$, where $P_i^j = (x_i^j, y_i^j)$ is the set of pixels on the contour. N is the number of pixels on the contour, and (x_i^j, y_i^j) represents the pixel on the contour. If the starting point and ending point of the contour are close, it is a closed contour; otherwise, it is an open contour.

$$A^j is \begin{cases} closed & if \left|\overline{P_1^j P_N^j}\right| < T, \\ open & if \left|\overline{P_1^j P_N^j}\right| > T, \end{cases} \tag{8}$$

The threshold T is used to determine whether two endpoints are close enough. In this paper, the value of T is set to 4.

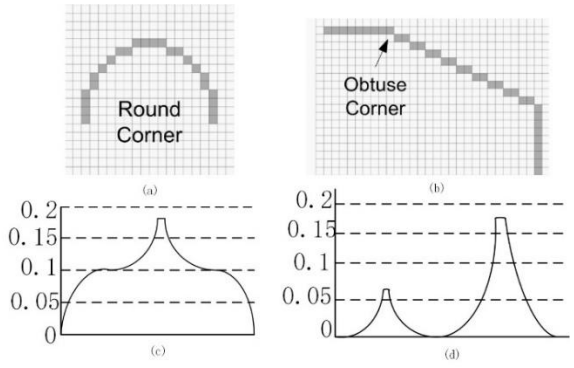

(a) Rounded corner (b) Obtuse angle (c) Curvature map of rounded corners in (a) (d) Curvature map of obtuse angles in (b)

Figure 6. Difference between rounded corners and obtuse angles.

The initial list of candidate corners includes all local maxima, although the maximum curvature of a rounded corner may not be significantly different from that of its neighborhood, as shown in (a) and (c) of the figure 6. Figure (b) has a curvature that is similar to a rounded corner but has a lower absolute maximum. Its size is usually significantly larger than that of its neighborhood, and the overall or global curvature features of its neighbors typically change more abruptly, as shown in (d) of the figure 6. To eliminate rounded corners rather than obtuse corners using the global curvature features of the neighborhood, the region of support(ROS) is defined.

The ROS of a corner is defined by the contour segment delimited by the two nearest minimum curvatures of the corner. A local threshold is adaptively computed using the ROS of each corner, where u is the position of the candidate corner on the contour, L1+L2 is the size of the ROS centered at u, and R is a coefficient.

$$T(u) = R \times \overline{K} = R \times \frac{1}{L_1 + L_2 + 1} \sum_{i=u-L_2}^{u+L_1} |K(i)| \tag{9}$$

In equation (9), $\overline{K}$ is the average curvature of the ROS. If the curvature of a corner is greater than $T(u)$, then it is considered a true corner; otherwise, it is removed from the list. This eliminates rounded corners because the rate of curvature decrease in L1+L2 is faster for obtuse angles than in the ROS region. Thus, the average curvature of an obtuse angle is smaller than that of a rounded corner, and the absolute curvature of a rounded corner is often less than $T(u)$, while that of an obtuse angle is often greater than $T(u)$, even if their absolute curvatures are similar. According to the experience in this paper, the coefficient R should be set to 1.5.

C. Removal of False Corners

In general, a clearly defined corner should have a relatively sharp angle. If the opening angle of each corner on the contour is known, a clear distinction can be made between true corners and false corners by using the following formula to calculate the corner opening angle.

$$\theta_u = \tan^{-1}\left(\frac{\Delta y_1}{\Delta x_1}\right) - \tan^{-1}\left(\frac{\Delta y_2}{\Delta x_2}\right) \tag{10}$$

$$\Delta x_1 = \frac{1}{L_1}\sum_{i=u+1}^{u+L_1} X(i) - X(u); \Delta y_1 = \frac{1}{L_1}\sum_{i=u+1}^{u+L_1} Y(i) - Y(u) \tag{11}$$

$$\Delta x_2 = \frac{1}{L_2}\sum_{i=u-L_2}^{u-1} X(i) - X(u); \Delta y_2 = \frac{1}{L_2}\sum_{i=u-L_2}^{u-1} Y(i) - Y(u) \tag{12}$$

u is the position of the corner to be judged, L_1 is the number of points between u and $u+1$, L_2 represents the number of points between u and $u-1$, and θ_u is the opening angle of the corner to be judged. If $160° \le \theta_u \le 200°$, the corner to be judged is removed.

3. EXPERIMENTS

To demonstrate the feasibility of the matching algorithm HOPCSS proposed in this paper, five sets of thermal infrared and visible images with different time periods, sensors, and experimental loads were selected as experimental samples. The experiments were implemented using Matlab software in a PC

This contribution has been peer-reviewed. The double-blind peer-review was conducted on the basis of the full paper.
https://doi.org/10.5194/isprs-annals-X-1-W1-2023-145-2023 | © Author(s) 2023. CC BY 4.0 License.

environment with a memory of 16 GB under the Win10 operating system. The selected images involve multiple test areas, including satellite images and unmanned aerial vehicle (UAV) images. In response to issues such as the sensitivity of the Harris operator to scale changes, this paper compared and analyzed the accuracy and precision of the matching algorithm HOPCSS proposed in this paper and the HOPC algorithm. Due to the different resolution of thermal infrared and visible images, the resolution of the two types of images will be different in the same area. The thermal infrared images need to be processed by Gaussian filtering to ensure that the two images are registered at the resolution size. This paper selected the correct match rate (CMR) and root-mean-square error (RMSE) as the evaluation indicators for image registration accuracy. CMR is an effective evaluation indicator. When the registration results of the matching algorithm are better, CMR will increase accordingly. RMSE is another precision evaluation indicator, which quantifies the matching accuracy by calculating the root mean square error of the corresponding image point in the matching algorithm results, making the experimental results more credible. Figure 7 shows the registration results of the proposed improved algorithm and the original algorithm. Table 1 summarizes the registration results obtained by the two matching algorithms for the five sets of thermal infrared and visible images.

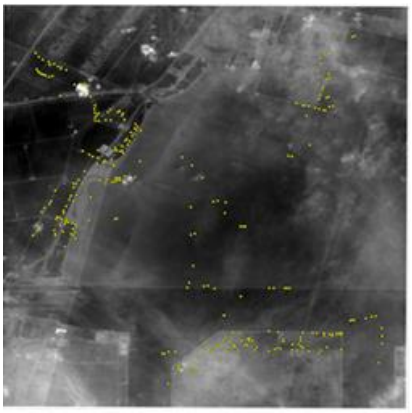

HOPC

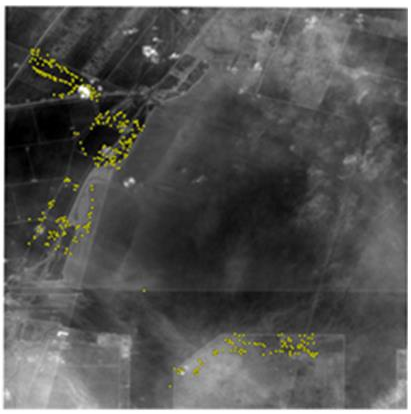

HOPCSS

Registration Result 1

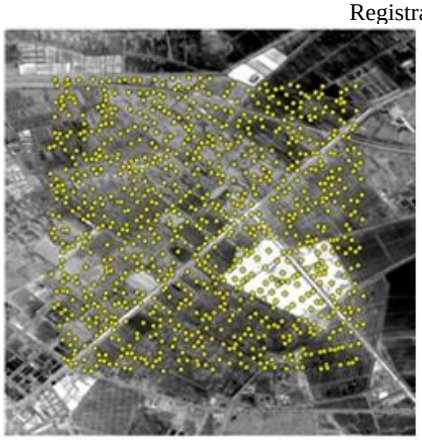

HOPC

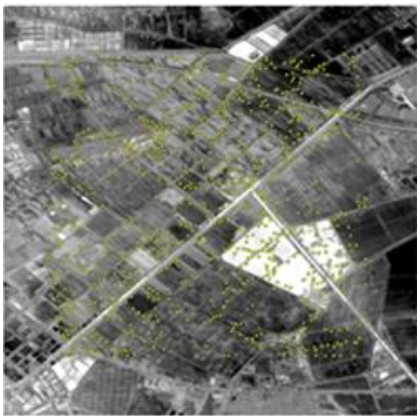

HOPCSS

Registration Result 2

HOPC

HOPCSS

Registration Result 3

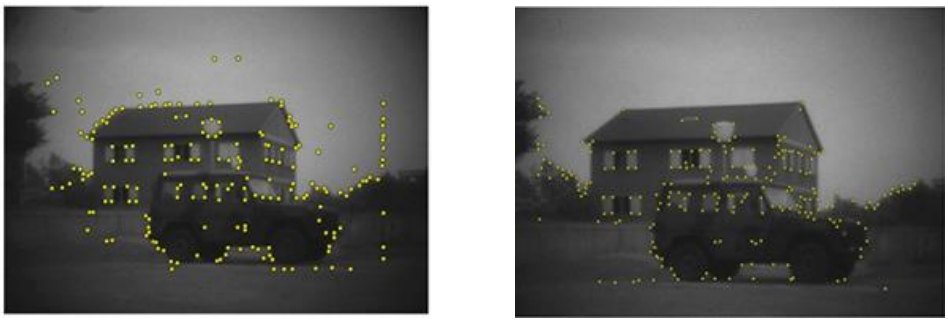

HOPC HOPCSS

Registration Result 4

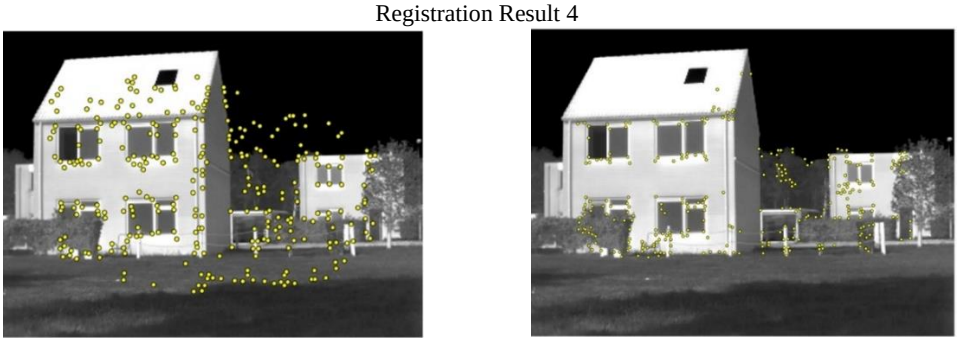

HOPC HOPCSS

Registration result 5

Figure 7. Registration of Experimental Image Data.

Thermal Infrared/Visible Image Pair	Method	Number of detected feature points	Number of coarse matching points	Number of fine matching points	CMR	RMSE (pixels)
Image group 1	HOPC	1400	272	91	0.334558	2.06
	HOPCSS	1373	367	114	0.310626	2.04
Image group 2	HOPC	1000	896	547	0.61049	1.96
	HOPCSS	988	926	582	0.62851	1.94
Image group 3	HOPC	700	651	501	0.76958	1.54
	HOPCSS	636	627	511	0.81499	1.39
Image group 4	HOPC	250	191	126	0.65968	1.82
	HOPCSS	230	230	164	0.71304	1.74
Image group 5	HOPC	360	300	151	0.50333	1.86
	HOPCSS	286	286	140	0.48951	1.78

Table 1. Evaluation metrics for different matching methods.

To verify the feasibility of the proposed algorithm HOPCSS, five groups of cross modality images with different sensor were applied for experiments. In Figure 7, image pairs (1/2) consist of GF-7/ZY3-03 panchromatic images and thermal infrared images, while image pairs (3/4/5) consist of high-resolution images taken by unmanned aerial vehicles(UAV).

In this paper, the GF-7 satellite, a domestically developed sub-meter optical stereoscopic mapping satellite, was successfully launched and put into operation in Taiyuan, China on November 3, 2019. the rear-view images from the panchromatic band ($0.45\sim0.90\ \mu m$) of the GF-7 satellite are used, with a resolution of $0.65\ m$. the ZY3-03 satellite, launched and put into operation in Taiyuan, China on July 15th, is a mapping satellite. the panchromatic images from the ZY3-03 satellite are used, with a resolution of $2.072\ m$. the thermal infrared remote sensing images have a resolution of $3\ m$, while the infrared resolution of the unmanned aerial vehicle (UAV) is $0.1\ m$.

In this paper, the improved algorithm HOPCSS, which combines CSS corner detection with phase congruency, was compared with the HOPC algorithm. By the matching results of multiple image groups, it was found that when the number of feature points detected by Harris was more than that detected by CSS, HOPCSS algorithm had higher matching accuracy than HOPC. In the registration results of HOPCSS, it can be seen that the corresponding image point are concentrated on the edge of the contour, while the feature points of HOPC are relatively evenly distributed. This is because the Harris operator used in HOPC algorithm can detect feature points even in blank areas of the image, which can lead to registration errors. In contrast, CSS corner detection detects the maximum curvature point of the contour and removes rounded corners and false corners, making corner detection more concentrated on the edge of the contour and avoiding corner extraction in the blank areas of the image, thereby effectively reducing noise interference in the image. In summary, the improved algorithm enhances registration accuracy and reduces a large number of invalid corresponding image point compared to the original algorithm.

In image group (1), the original algorithm and the improved algorithm extracted 1400 and 1373 feature points, respectively. However, the HOPCSS algorithm had more accurate matching points than the HOPC algorithm. It is worth noting that the matching points detected by the HOPCSS algorithm are distributed mainly at the edges and areas with significant

curvature changes, with few in blank areas. Compared with image pairs (3/4/5), the improvement in satellite image registration was little, while the improvement in UAV image registration was more significant. This is likely due to the resolution of the thermal infrared and panchromatic images by the UAV was higher and without Gaussian blur, resulting in better registration effects. Compared with the HOPC algorithm, the proposed method performed better in matching results. Combining the table 1 and the figure 7, it can be seen that the proposed method has certain robustness. In summary, this paper studied the registration of thermal infrared and visible images, and the results showed that whether in satellite or UAV images, the HOPCSS algorithm had a significant increasement in the number of corresponding image point compared with the HOPC algorithm, and had significant advantages in matching accuracy.

4. CONCLUSION

This paper proposes an improved image registration algorithm based on geometric structure attributes for thermal infrared and visible images with large radiometric differences. Firstly, the HOPC feature vector is constructed based on the phase congruency principle, and then the main image CSS feature points are extracted. The CSS corner detection algorithm is combined with geometric structure descriptors to propose the HOPCSS algorithm for the registration of images. The advantages of CSS corner detection are expressed, and the following conclusions are drawn:

(1) Through analysis of selected satellite images, unmanned aerial vehicle (UAV) images, and professional camera images, it was found that when detecting a smaller number of feature points, the proposed algorithm in this paper had more accurately matched points and overall higher accuracy than the original algorithm.

(2) The registration results show that many of the corresponding image points matched by the original algorithm are distributed in the blank areas of the images, resulting in the generation of invalid corresponding image points. In contrast, the corresponding image points by the proposed algorithm in this paper are more concentrated around the contours of the images, reducing the number of invalid corresponding image points. From this perspective, the improved algorithm proposed in this paper can to some extent resist noise interference.

(3) Through the analysis of the principle of matching algorithms, it is found that in order to automatically register images with large radiation differences, it is necessary to start from the structural similarity of the two images and then perform matching.

The algorithm proposed in this paper still has room for improvement and areas that require further refinement, providing potential research directions and opportunities for improvement.

(1) When using the HOPCSS algorithm proposed in this paper for the registration of heterogeneous remote sensing images, it is necessary to apply Gaussian blurring to the images to ensure that both images are at the same resolution. The matching performance may be affected when the resolutions of the two images are different. Future research can explore matching algorithms for heterogeneous remote sensing images at different resolutions.

(2) The algorithm proposed in this paper cannot handle heterogeneous remote sensing images with significant rotation angles. Future research can explore matching algorithms for heterogeneous remote sensing images with large rotation angles.

ACKNOWLEDGEMENTS

This work was partly supported by the National Key R&D Program of China (2020YFE0200800), the National Natural Science Foundation of China (41971426), the Multibeam Laser Terrain Detection Radar and Application Technology (D040105), the Special Funds for Creative Research (2022C61540). the Innovative Youth Talents Program, Ministry of Natural Resources of the People's Republic of China (12110600000018003930), and independent research program of key Laboratory of Land Satellite Remote Sensing Application, MNR, NO.BN2302-6.

REFERENCES

Bai, Z., Li, G., & Liu, Z., 2023. Global–local–global context-aware network for salient object detection in optical remote sensing images. *ISPRS Journal of Photogrammetry and Remote Sensing*, 198, 184-196.

Blaschke, T., 2010. Object based image analysis for remote sensing. *ISPRS journal of photogrammetry and remote sensing*, 65(1), 2-16.

Chen, J., Cheng, B., Zhang, X., Long, T., Chen, B., Wang, G., & Zhang, D., 2022. A TIR-Visible Automatic Registration and Geometric Correction Method for SDGSAT-1 Thermal Infrared Image Based on Modified RIFT. *Remote Sensing*, 14(6), 1393.

Canny, J., 1986. A computational approach to edge detection. *IEEE Transactions on pattern analysis and machine intelligence*, (6), 679-698.

Dematteis, N., Giordan, D., Zucca, F., Luzi, G., & Allasia, P., 2018. 4D surface kinematics monitoring through terrestrial radar interferometry and image cross-correlation coupling. *ISPRS journal of photogrammetry and remote sensing*, 142, 38-50.

Deng, L., Mao, Z., Li, X., Hu, Z., Duan, F., & Yan, Y., 2018. UAV-based multispectral remote sensing for precision agriculture: A comparison between different cameras. ISPRS journal of photogrammetry and remote sensing, 146, 124-136.

Fischler, M. A., Bolles, R. C., 1981. Random sample consensus: a paradigm for model fitting with applications to image analysis and automated cartography. *Communications of the ACM*, 24(6), 381-395.

Foody, G. M., 2002. Status of land cover classification accuracy assessment. *Remote sensing of environment*, 80(1), 185-201.

Gao, J., Liu, J., & Ji, S., 2023. A general deep learning based framework for 3D reconstruction from multi-view stereo satellite images. *ISPRS Journal of Photogrammetry and Remote Sensing*, 195, 446-461.

Gong, J., Liu, C., & Huang, X., 2020. Advances in urban information extraction from high-resolution remote sensing imagery. *Science China Earth Sciences*, 63, 463-475.

Harris, C., & Stephens, M., 1988. A combined corner and edge detector. *In Alvey vision conference* (Vol. 15, No. 50, pp. 10-5244).

Hu, Q., Zhen, L., Mao, Y., Zhou, X., & Zhou, G., 2021. Automated building extraction using satellite remote sensing imagery. *Automation in Construction*, 123, 103509.

Han, L., Shi, L., Yang, Y., & Song, D., 2014. Thermal physical property-based fusion of geostationary meteorological satellite visible and infrared channel images. *Sensors*, 14(6), 10187-10202.

Ye, Y., Shan, J., 2014. A local descriptor based registration method for multispectral remote sensing images with non-linear intensity differences. *ISPRS Journal of Photogrammetry and Remote Sensing*, 90, 83-95.

Yu, Q., Ni, D., Jiang, Y., Yan, Y., An, J., Sun, T., 2021. Universal SAR and optical image registration via a novel SIFT framework based on nonlinear diffusion and a polar spatial-frequency descriptor. *ISPRS Journal of Photogrammetry and Remote Sensing*, 171, 1-17.

Yu, Z., Juanjuan, Z., Rui, L., & Haidong, Z., 2021. Registration of thermal infrared image and visible image based on featured contour quadrilateral. Infrared And Laser Engineering, 50(S2), 20200520-1.

Jiang Qian, Liu Yadong, Fang Jian, Yan Yingjie1, Jiang Xiuchen, 2020. Registration method for power equipment infrared and visible images based on contour feature. *Chinese Journal of Scientific Instrument*, 41(11), 252-260.

Joshi, N., Baumann, M., Ehammer, A., Fensholt, R., Grogan, K., Hostert, P., ... & Waske, B., 2016. A review of the application of optical and radar remote sensing data fusion to land use mapping and monitoring. *Remote Sensing*, 8(1), 70.
Kovesi, P., 1999. Image features from phase congruency. *Videre: Journal of computer vision research*, 1(3), 1-26.

Li, S., Wang, W. C., & Li, L. W., 2013. Advances on Urban Impervious Surface Extraction Using Remote Sensing Data. *In Advanced Materials Research* (Vol. 726, pp. 4552-4557). Trans Tech Publications Ltd.

Lowe, D. G., 2004. Distinctive image features from scale-invariant keypoints. *International journal of computer vision*, 60, 91-110.

Masouleh, M. K., & Shah-Hosseini, R., 2019. Development and evaluation of a deep learning model for real-time ground vehicle semantic segmentation from UAV-based thermal infrared imagery. *ISPRS Journal of Photogrammetry and Remote Sensing*, 155, 172-186.

Quddus, A., Fahmy, M. M., 1999. An improved wavelet-based corner detection technique. In 1999 IEEE International Conference on Acoustics, Speech, and Signal Processing. Proceedings. ICASSP99 (Cat. No. 99CH36258) (Vol. 6, pp. 3213-3216). IEEE.

Rahaghi, A. I., Lemmin, U., Sage, D., & Barry, D. A., 2019. Achieving high-resolution thermal imagery in low-contrast lake surface waters by aerial remote sensing and image registration. *Remote Sensing of Environment*, 221, 773-783.
Ramat, G., Santi, E., Paloscia, S., Fontanelli, G., Pettinato, S., Santurri, L., ... & Lili Chabaane, Z., 2023. Remote sensing techniques for water management and climate change monitoring in drought areas: case studies in Egypt and Tunisia. *European Journal of Remote Sensing*, 56(1), 77-99.

Mokhtarian, F., Bober, M., Mokhtarian, F., & Bober, M., 2003. Robust image corner detection through curvature scale space. *Curvature Scale Space Representation: Theory, Applications, and MPEG-7 Standardization*, 215-242.

Song, D. X., Huang, C., Sexton, J. O., Channan, S., Feng, M., & Townshend, J. R., 2015. Use of Landsat and Corona data for mapping forest cover change from the mid-1960s to 2000s: Case studies from the Eastern United States and Central Brazil. *ISPRS Journal of Photogrammetry and Remote Sensing*, 103, 81-92.

Sobrino, J. A., Jiménez-Muñoz, J. C., & Paolini, L., 2004. Land surface temperature retrieval from LANDSAT TM 5. *Remote Sensing of environment*, 90(4), 434-440.

Weng, Q., 2009. Thermal infrared remote sensing for urban climate and environmental studies: Methods, applications, and trends. *ISPRS Journal of photogrammetry and remote sensing*, 64(4), 335-344.

Wang, S., Sun, L., Gao, Y., & Cheng, R., 2020. Application of Multi-Sensor Based Image Modeling in Ocean Remote Sensing. *Journal of Coastal Research*, 107(SI), 125-128.

WANG Mengmeng, YE Yuanxin, ZHU Bai1, ZHANG Guo, 2022. An Automatic Registration Method for Optical and SAR Images Based on Spatial Constraint and Structure Features. Geomatics and Information Science of Wuhan University, 47(1), 141-148.

Valero, S., Ceccato, P., Baethgen, W. E., & Chanussot, J., 2013. Identification of agricultural crops in early stages using remote sensing images. *In 2013 IEEE International Geoscience and Remote Sensing Symposium-IGARSS* (pp. 4229-4232). IEEE.

XI Shaoli,LI Wei, XIE Junfeng, MO Fan,. 2020. Feature Point Matching Between Infrared Image and Visible Light Image Based on SIFT and ORB Operators. Infrared Technology, 42(2), 168.

YE Yuan-Xin, HAO Si-Yuan, CAO Yun-Gang, 2017. Automatic registration of optical and SAR image using geometric structural properties. Journal of Infrared and Millimeter Waves, 36(6), 720-726.

Zhao, Y., Wu, B., Li, Q., Yang, L., Fan, H., Wu, J., & Yu, B., 2023. Combining ICESat-2 photons and Google Earth Satellite images for building height extraction. *International Journal of Applied Earth Observation and Geoinformation*, 117, 103213.

Zitova, B., & Flusser, J., 2003. Image registration methods: a survey. *Image and vision computing*, 21(11), 977-1000.

Zhang, Z., Lu, L., Zhao, Y., Wang, Y., Wei, D., Wu, X., & Ma, X., 2023. Recent advances in using Chinese Earth observation satellites for remote sensing of vegetation. *ISPRS Journal of Photogrammetry and Remote Sensing*, 195, 393-407.

Zhang, R., Zhang, H., Ning, X., Huang, X., Wang, J., & Cui, W., 2023. Global-aware siamese network for change detection on remote sensing images. *ISPRS Journal of Photogrammetry and Remote Sensing*, 199, 61-72.